

# HACA3: A unified approach for multi-site MR image harmonization

Lianrui Zuo<sup>1,2</sup>[0000-0002-5923-9097], Yihao Liu<sup>1</sup>, Yuan Xue<sup>1</sup>, Blake E. Dewey<sup>3</sup>, Murat Bilgel<sup>2</sup>, Ellen M. Mowry<sup>3</sup>, Scott D. Newsome<sup>3</sup>, Peter A. Calabresi<sup>3</sup>, Susan M. Resnick<sup>2</sup>, Jerry L. Prince<sup>1</sup>, and Aaron Carass<sup>1</sup>

<sup>1</sup> Department of Electrical and Computer Engineering,  
Johns Hopkins University, Baltimore, MD 21218, USA

<sup>2</sup> Laboratory of Behavioral Neuroscience, National Institute on Aging,  
National Institutes of Health, Baltimore, MD 20892, USA

<sup>3</sup> Department of Neurology,  
Johns Hopkins School of Medicine, Baltimore, MD 21287, USA

**Abstract.** The lack of standardization is a prominent issue in magnetic resonance (MR) imaging. This often causes undesired contrast variations due to differences in hardware and acquisition parameters. In recent years, MR harmonization using image synthesis with disentanglement has been proposed to compensate for the undesired contrast variations. Despite the success of existing methods, we argue that three major improvements can be made. First, most existing methods are built upon the assumption that multi-contrast MR images of the same subject share the same anatomy. This assumption is questionable since different MR contrasts are specialized to highlight different anatomical features. Second, these methods often require a fixed set of MR contrasts for training (e.g., both  $T_1$ -weighted and  $T_2$ -weighted images must be available), which limits their applicability. Third, existing methods generally are sensitive to imaging artifacts. In this paper, we present a novel approach, Harmonization with Attention-based Contrast, Anatomy, and Artifact Awareness (HACA3), to address these three issues. We first propose an anatomy fusion module that enables HACA3 to respect the anatomical differences between MR contrasts. HACA3 is also robust to imaging artifacts and can be trained and applied to any set of MR contrasts. Experiments show that HACA3 achieves state-of-the-art performance under multiple image quality metrics. We also demonstrate the applicability of HACA3 on downstream tasks with diverse MR datasets acquired from 21 sites with different field strengths, scanner platforms, and acquisition protocols.

**Keywords:** MRI · Disentanglement · Attention · Harmonization · Contrastive learning

## 1 Introduction

Magnetic resonance (MR) imaging is a non-invasive and flexible imaging modality that is commonly used to study the human brain. By modifying the underlying

pulse sequences, multiple MR tissue contrasts can be acquired in a single imaging session to reveal different tissue properties and pathology [19]. This flexibility of MR imaging also comes with drawbacks, most notably the lack of standardization between imaging studies. Changes in pulse sequences, imaging parameters, and scanner manufacturers often cause undesired contrast variations in acquired images. These contrast variations are commonly seen in multi-site and longitudinal studies, where acquiring images with identical protocols and parameters is difficult. It has been shown that directly processing these images without compensating for the contrast variations can lead to biased and inconsistent measurements (also known as the domain shift problem) [3,6].

*Harmonization through image synthesis alleviates domain shift.* In recent years, image synthesis-based MR harmonization techniques [7,9,14,31,32] have been proposed to mitigate the lack of standardization in MR imaging. These methods are a special type of image-to-image translation (I2I) [11,18,29,30], with the source and target images  $x$  and  $y$  coming from different sites (e.g., T<sub>1</sub>-w images from two sites). Here, we assume images acquired with the same hardware and software come from the same (imaging) site. These methods learn a function  $f(\cdot)$  that translates  $x$  from a source site to a target site, i.e.,  $\hat{y} = f(x)$  while preserving the underlying anatomy. Depending on the requirement on training data, existing harmonization methods can be categorized into supervised and unsupervised methods. Supervised harmonization methods [7,23] require a sample population to be imaged at multiple sites. The acquired images across sites (inter-site paired data) are then used to train  $f(\cdot)$ . Although supervised harmonization generally has superior performance due to the explicit supervision provided by the inter-site paired data, their application is limited to sites visited by traveling subjects. Unsupervised harmonization methods do not require inter-site paired data, thus they usually have broader applicability. Most existing unsupervised I2I methods such as CycleGAN [29], MUNIT [11], and CUT [18] can be used to achieve unsupervised harmonization. However, geometry shift of unsupervised I2I methods is an outstanding problem due to the absence of supervision on anatomy across sites.

*A unique aspect of MR imaging motivates better unsupervised harmonization.* A unique aspect of MR imaging is that multi-contrast images of the same subject (intra-site paired data) are routinely acquired in a single imaging session. In recent years, unsupervised harmonization methods with disentanglement have been proposed to utilize intra-site paired data to achieve better harmonization. The core concept is to disentangle anatomical and contrast (i.e., acquisition related) information using intra-site paired images during training, so that the anatomy information and a desired contrast can be recombined at test time to achieve inter-site harmonization. Zuo et al. [31] disentangled anatomical and contrast information given intra-site paired T<sub>1</sub>-w and T<sub>2</sub>-w images. In their work, disentanglement was achieved with adversarial training and a similarity loss, assuming the intra-site paired images share the same anatomy. Ouyang et al. [17] learned disentangled anatomy and contrast representations based on intra-site paired data with a margin hinge loss. The authors reported superior performance

over existing unsupervised I2I methods such as CycleGAN [29], due to the supervision in geometry provided by the intra-site paired data.

*Current harmonization methods miss an important consideration.* Most disentangling methods assume the intra-site paired images share identical underlying anatomy while only differing in image contrast [5, 8, 31]. This assumption is commonly used as an inductive bias, which is fundamental to learn disentanglement [16]. However, a missing consideration is that different MR contrasts are specifically designed to better reveal different pathology, meaning that the identical anatomy assumption is not strictly true in MR imaging. Recent works [17, 33] have reported on the negative impact of enforcing identical anatomies of intra-site paired data. Despite their efforts, there remains multiple unresolved problems with training a harmonization model that respects the anatomical differences between MR images with different acquisitions. First, the observable anatomy of intra-site paired images should be considered different, so we need a new inductive bias to achieve disentanglement. Second, the MR tissue contrasts from the source site have an impact on harmonization. Ideally, the model should understand MR tissue contrast and choose an appropriate combination of contrasts to produce a better harmonization. Third, imaging artifacts and missing contrasts should be handled to improve robustness and applicability.

In this paper, we propose a novel harmonization approach that resolves the three issues with attention-based contrast, anatomy, and artifact awareness (HACA3). The contributions of the paper are as follows: First, we challenge the common assumption of disentanglement and propose a new inductive bias to learn disentanglement from MR images. As a result, HACA3 respects the natural anatomy difference between MR contrasts. Second, we design a novel contrast and artifact attention mechanism to produce an optimal harmonized image based on the contrast and artifact information of each input image. Third, HACA3 can be trained and applied to any set of MR contrasts by using a special design to handle missing contrasts. HACA3 outperforms existing harmonization and I2I methods according to multiple image quality metrics. We use diverse MR datasets to demonstrate the broad applicability of HACA3 in downstream tasks including WM lesion segmentation and whole brain parcellation.

## 2 Methods

### 2.1 General framework

HACA3 has an “encoder–attention–decoder” structure. Different from existing frameworks that disentangle anatomy and contrast [8, 15, 17, 32], HACA3 has an additional encoder—the artifact encoder—to assess the extent of artifacts in the input MR images. We also introduce an attention module that analyzes the learned representations of contrast, anatomy, and artifacts to inform the decoder for better harmonization. Figure 1 shows the schematic framework of HACA3. In this section, we describe general ideas of HACA3. We provide detailed explanations of the encoding and attention steps in Secs. 2.2 and 2.3, respectively. During training, intra-site  $T_1$ -w,  $T_2$ -w, proton density weighted (PD-w), and

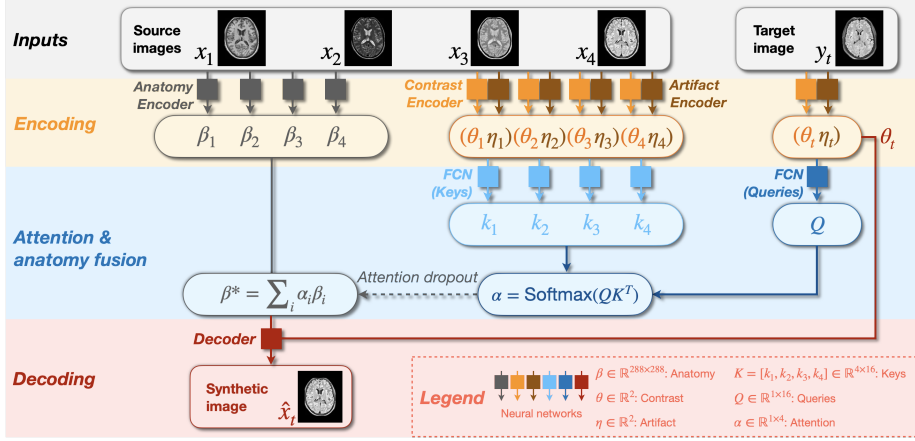


**Fig. 1.** Schematic framework of HACA3. Networks with the same color share weights. Synthetic image  $\hat{x}_t$  has the same contrast as the target image  $y_t$  while preserving the anatomy from source images.

T<sub>2</sub>-w fluid-attenuated inversion recovery (FLAIR) images (denoted respectively as  $x_1, x_2, x_3$ , and  $x_4$ ) of the same subject are individually encoded into anatomy representations  $\beta$ , contrast representations  $\theta$ , and artifact representations  $\eta$ , with the corresponding encoders  $E_\beta(\cdot)$ ,  $E_\theta(\cdot)$ , and  $E_\eta(\cdot)$ . Note that HACA3 does not require all four contrasts for training; it can be trained with any combination of MR tissue contrasts, as we describe in Sec. 2.3. Contrast  $\theta_t$  and artifact  $\eta_t$  representations of the target image  $y_t$  are also calculated during encoding.

Following [5, 8, 17, 31, 33], HACA3 conducts intra-site I2I (e.g., intra-site T<sub>1</sub>-w to T<sub>2</sub>-w synthesis) with disentangled representations  $\theta$  and  $\beta$  during training. At test time,  $\theta$  and  $\beta$  are recombined (usually from different sites) to achieve inter-site harmonization. The anatomy representation  $\beta$  has the same spatial dimension as images  $x$  with five distinct intensity levels, which are calculated from a five-channel one-hot encoded map. The contrast representation  $\theta$  and artifact representation  $\eta$  are two-dimensional variables (i.e.,  $\theta, \eta \in \mathbb{R}^2$ ). The learned representations  $\theta$  and  $\eta$  are then processed by an attention module (which we describe in Sec. 2.3) to find the optimal fused anatomy representation  $\beta^*$  based on the desired contrast of target image  $y_t$ . The decoder then recombines  $\beta^*$  and  $\theta_t$  to generate a harmonized image  $\hat{x}_t$  with the desired contrast as  $y_t$  while preserving the anatomy from the source images.

## 2.2 Encoding: contrast, anatomy, and artifacts

**A novel way to disentangle anatomy and contrast.** We introduce a novel way to disentangle anatomy and contrast while respecting the natural anatomy discrepancy between different MR contrasts. The core concept of our anatomy encoder is based on contrastive learning [18], which learns discriminative features



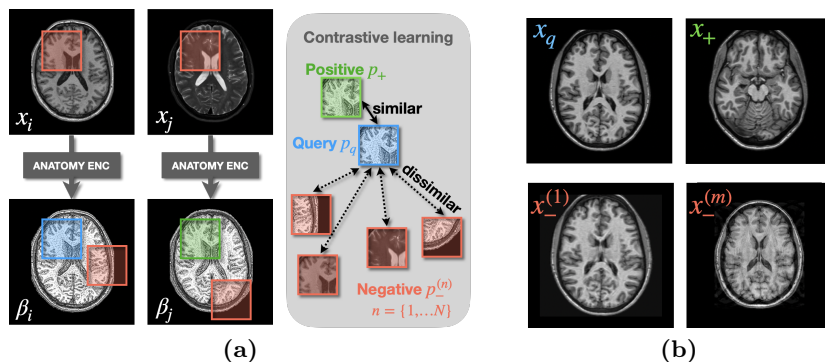


**Fig. 2.** (a) Learning anatomical representation based on contrastive learning.  $p_q$ ,  $p_+$ , and  $p_-^{(n)}$  are query patch, positive patch, and negative patches, respectively.  $p_q$  is encouraged to be more similar to  $p_+$  than to  $p_-^{(n)}$  using Eq. 1, where  $n = \{1, \dots, N\}$  and  $N$  is the number of negative patches. (b) Example images for training artifact encoder  $E_\eta(\cdot)$ , where  $x_q$  and  $x_+$  have similar levels of artifact as  $x_-^{(m)}$ .

from query, positive, and negative examples. Here, the query, positive, and negative examples are image patches denoted as  $p_q$ ,  $p_+$ , and  $p_-$ , respectively. As shown in Fig. 2, intra-site paired images are individually processed by the anatomy encoder to learn anatomical representations, where  $i, j \in \{1, 2, 3, 4\}$  ( $i \neq j$ ) are contrast indexes randomly selected from all available MR contrasts. The query patch,  $p_q$ , is selected at a random location of  $\beta_i$ . The positive patches  $p_+$  are selected at the corresponding locations of  $\beta_j$ , where  $j \neq i$ . Negative patches  $p_-^{(n)}$  are sampled at the same locations as  $p_q$  from the original images as well as random locations from the learned  $\beta$ 's. Instead of enforcing  $p_q$  to be identical to  $p_+$ , we encourage  $p_q$  to be more similar to  $p_+$  than to the  $p_-^{(n)}$ 's using

$$\mathcal{L}_c(p_q, p_+, p_-^{(n)}) = -\log \left[ \frac{\exp(p_q \cdot p_+)}{\exp(p_q \cdot p_+) + \frac{1}{N} \sum_{n=1}^N \exp(p_q \cdot p_-^{(n)})} \right]. \quad (1)$$

Our inductive bias is that no matter how similar  $p_q$  and  $p_-^{(n)}$ 's are, the positive patches  $p_+$  should always be more similar to  $p_q$ , but not necessarily identical. The intuition is that  $p_q$  and  $p_+$  are representations of the same subject, while  $p_-^{(n)}$ 's either represent different anatomical information or the same subject with weighted contrasts. Equation 1 essentially encourages contrast information to be removed from  $\beta$ . Because our decoder takes both  $\beta$  and  $\theta$  as direct inputs to generate a harmonized image during training, thus contrast information is pushed to the  $\theta$  branch, which we adopt from [32].

**Learning representations of artifacts.** Our artifact encoder  $E_\eta(\cdot)$  is designed to capture the extent of artifact  $\eta$  from source MR images  $x$ , i.e.,  $\eta = E_\eta(x)$ , so that the harmonization model is informed to avoid using images with high levels of artifacts.  $E_\eta(\cdot)$  is also based on contrastive learning, with query, positive, and negative examples being MR images denoted as  $x_q$ ,  $x_+$ , and  $x_-^{(m)}$ , respectively.

We prepare  $x_q$  and  $x_+$  by selecting 2D image slices from the same 3D MR volume, assuming they have similar levels of artifact. Negative examples  $x_-^{(m)}$  are prepared by 1) augmenting  $x_q$  by introducing simulated artifacts, like motion and noise, and 2) by selecting 2D image slices from different volumes than  $x_q$ . Example images for training  $E_\eta(\cdot)$  are shown in Fig. 2(b). In both ways, we assume  $x_-^{(m)}$ 's and  $x_q$  have different artifact levels. The final loss to train  $E_\eta(\cdot)$  is given by the contrastive loss  $\mathcal{L}_C(\eta_q, \eta_+, \eta_-^{(m)})$  in Eq. 1, where  $m = \{1, \dots, M\}$ .

### 2.3 Decoding with attention

**Attention and anatomy fusion.** Due to the nature of MR imaging,  $\beta_i$ 's ( $i = \{1, 2, 3, 4\}$ ) from different images of the same subject should be similar but not necessarily identical. Therefore, the choice of  $\beta_i$  during decoding has an impact on harmonization. Given an MR contrast from a target site, it is intuitive to choose  $\beta$  of the same contrast from the source site since similar pulse sequences usually reveal similar underlying anatomical information. However, an alternative is to calculate  $\beta$ 's from all the available contrasts of the source images, since this provides increased robustness against imaging artifacts and poor image quality in any of the source images. Previous work [5, 17, 31] has approached image synthesis in both ways, but HACA3 takes a step further by combining the merits of both ways. We propose a novel attention mechanism that takes both contrast and artifact into consideration when fusing anatomy from multiple source images. The encoded  $\theta$  and  $\eta$  from both source and target images are processed by fully connected networks to learn keys  $K = [k_1, k_2, k_3, k_4]$  and queries  $Q$  [26], as shown in Fig. 1. Attentions  $\alpha \in \mathbb{R}^4$  are then obtained by measuring the similarity between  $K$  and  $Q$ . Here we assume the  $y_t$  being used as harmonization target in training has good image quality, and the learned attentions will highlight corresponding source images that have similar contrast and image quality as  $y_t$ . The optimal anatomical representation,  $\beta^*$ , is then obtained by conducting a weighted average with attention, i.e.,  $\beta^* = \sum_{i=1}^4 \alpha_i \beta_i$ . The decoder combines both  $\beta^*$  and  $\theta_t$  to generate a synthetic image  $\hat{x}_t$ . To enable HACA3 to handle arbitrary numbers of MR contrasts during training, we introduce an attention dropout mechanism. When there are missing contrasts during training, the corresponding dimensions of  $\alpha$  are set to zero and  $\alpha$  is renormalized, so that  $\sum_{i=1}^4 \alpha_i = 1$  and  $\beta$  of the missing contrasts will not be selected to calculate  $\beta^*$ . Even when all four contrasts are available during training, one or more dimensions of  $\alpha$  have a chance to be randomly dropped out (set to zero) and  $\alpha$  is renormalized.

**Loss functions.** The framework of HACA3 is a conditional variational auto-encoder (CVAE) with  $\theta$  being the latent variable. The condition of the CVAE is  $\beta^*$ . The CVAE loss to train HACA3 is given by  $\mathcal{L}_{\text{CVAE}} = |\hat{x}_t - y_t|_1 + \mathcal{D}_{\text{KL}}[p(\theta|y_t)||p(\theta)]$ , where  $\mathcal{D}_{\text{KL}}$  is the KL divergence. To further regularize HACA3, synthetic image  $\hat{x}$  is then reanalyzed by the encoders  $E_\theta(\cdot)$  and  $E_\eta(\cdot)$  and a cycle consistency loss is calculated, i.e.,  $\mathcal{L}_{\text{cyc}} = |E_\theta(\hat{x}_t) - \theta_t|_1 + |E_\eta(\hat{x}_t) - \eta_t|_1$ . The overall loss to train HACA3 includes  $\mathcal{L}_{\text{CVAE}}$ , contrastive losses for anatomy and artifact encoders (see

**Table 1.** MR images acquired from 21 sites were used to train and evaluate HACA3. Out of the 21 sites, 11 are publicly available [1, 4, 13, 21]. Manufacturer keys: P - Philips; S - Siemens; G - GE. Magnetic field strengths are reported in Tesla.

Site ID	$S_1$	$S_2$	$S_3$	$S_4$	$S_5$	$S_6$	$S_7$	$S_8$	$S_9$	$S_{10}$	$S_{11}$	$S_{12}$	$S_{13}$	$S_{14}$	$S_{15}$	$S_{16}$	$S_{17}$	$S_{18}$	$S_{19}$	$S_{20}$	$S_{21}$	
Open data	✓	✓	✓	✓	✓	✓	✓	✓	✓	✓	✓	✗	✗	✗	✗	✗	✗	✗	✗	✗	✗	
Manufacturer	P	P	S	S	S	S	P	P	P	P	P	P	S	G	S	G	P	S	S	S	S	
Field	1.5	3.0	3.0	3.0	3.0	1.5	1.5	3.0	3.0	3.0	3.0	3.0	3.0	1.5	3.0	3.0	3.0	3.0	3.0	1.5	3.0	
T <sub>1</sub> -w	✓	✓	✓	✓	✓	✓	✓	✓	✓	✓	✓	✓	✓	✓	✓	✓	✓	✓	✓	✓	✓	✓
T <sub>2</sub> -w	✓	✓	✓	✓	✓	✓	✓	✓	✓	✓	✓	✓	✓	✓	✓	✓	✓	✓	✓	✓	✓	✓
PD-w	✓	✓	✗	✗	✗	✗	✓	✓	✓	✓	✓	✓	✓	✗	✓	✓	✓	✓	✓	✓	✗	✓
FLAIR	✗	✗	✗	✗	✗	✗	✓	✓	✓	✓	✓	✓	✓	✓	✓	✓	✓	✓	✓	✓	✓	✓

Eq. 1), and  $\mathcal{L}_{\text{cyc}}$ , i.e.,

$$\mathcal{L}_{\text{total}} = \lambda_1 \mathcal{L}_{\text{CVAE}} + \lambda_2 \mathcal{L}_{\text{C}}(p_q, p_+, p_-^{(n)}) + \lambda_3 \mathcal{L}_{\text{C}}(\eta_q, \eta_+, \eta_-^{(m)}) + \lambda_4 \mathcal{L}_{\text{cyc}}, \quad (2)$$

where  $\lambda$ 's are hyperparameters. During training, target image  $y_t$  is first randomly selected from intra-site paired images  $x_1$  to  $x_4$ . In this case, HACA3 is trained to conduct intra-site I2I with disentanglement. We also select  $y_t$  from a different site than the source images during training. In this case, only  $\mathcal{L}_{\text{cyc}}$  is calculated to train the attention module with inter-site I2I.

**Implementation details.** Our anatomy encoder and decoder are both U-Net's [22] with four downsampling layers. The contrast encoder is a fully convolutional network with four ‘‘Conv–InstanceNorm–LeakyReLU’’ modules. Our artifact encoder has a ResNet structure with four convolutional layers.

### 3 Experiments and Results

HACA3 is developed and evaluated with highly variable MR datasets acquired from 21 sites. Key information about data source, acquisition, and manufacturer is shown in Table 1. These datasets include healthy subjects (Sites  $S_1$  to  $S_{10}$ ) and subjects with multiple sclerosis (MS) (Sites  $S_{11}$  to  $S_{21}$ ). Images were pre-processed with inhomogeneity correction [25], super-resolution for 2D acquired images [28], registration to an MNI atlas with 0.8mm<sup>3</sup> resolution, and a WM peak normalization [20]. Ten training and two validation subjects (with two to four MR contrasts for each subject, depending on the availability) from each site were selected. HACA3 was then trained with 2D axial, coronal, and sagittal slices extracted from each 3D MR volume. We adopt the model introduced in [32] to combine 2D slices into 3D volumes as our final harmonization result.

#### 3.1 Multi-site MR harmonization

In this experiment, we seek a harmonization model that translates T<sub>1</sub>-w images from a source site to a target site. We used a held-out dataset with 12 subjects traveling across sites  $S_{11}$  (source) and  $S_{12}$  (target) to quantitatively

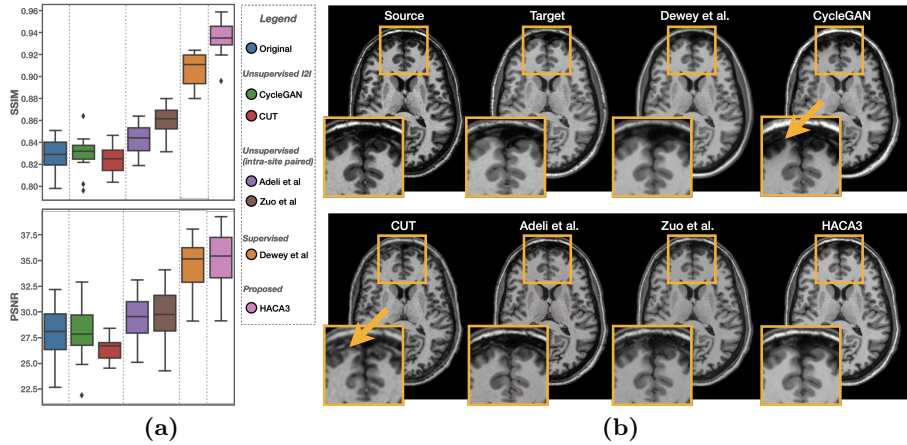


**Fig. 3.** (a) Numerical comparisons between HACA3 (proposed) and other methods using a held-out dataset with inter-site traveling subjects. SSIM and PSNR of T<sub>1</sub>-w images are calculated. Example T<sub>1</sub>-w images are shown in (b).

evaluate HACA3 and other methods. These methods come from three broad types: 1) unsupervised I2I including CycleGAN [29] and CUT [18], 2) two unsupervised harmonization methods based on intra-site paired data [2, 32], and 3) supervised harmonization [7]. Structural similarity index (SSIM) [27] and peak signal-to-noise ratio (PSNR) are used to quantitatively evaluate all methods.

*Compared with unsupervised I2I with cycle consistency:* As shown in Fig. 3(a), we first compared HACA3 (pink) with CycleGAN (green) and CUT (red). Both CycleGAN and CUT were trained on unpaired T<sub>1</sub>-w images from Sites  $S_{11}$  and  $S_{12}$ . HACA3 outperforms both methods with statistical significance ( $p < 0.01$  in a paired Wilcoxon signed rank test). Surprisingly, CycleGAN and CUT did not show much improvements compared with the unharmonized images (blue), although the synthetic images are visually good, as shown in Fig. 3(b). We hypothesize that this is due to the issue of geometry shift, as highlighted by the orange arrows in Fig. 3(b). This demonstrates the cycle consistency constraint for anatomy is not sufficient for MR harmonization.

*Compared with unsupervised harmonization based-on intra-site paired data:* We then compared HACA3 to existing unsupervised harmonization methods which are also built upon intra-site paired data. Both Adeli et al. [2] and Zuo et al. [32] were trained on intra-site paired T<sub>1</sub>-w and T<sub>2</sub>-w images with disentanglement. As shown in Fig. 3(a), HACA3 outperforms these methods with statistical significance ( $p < 0.01$  in a paired Wilcoxon signed rank test). Considering that all three methods are based on intra-site paired images, we believe that the superior performance of HACA3 comes from the ability to use multiple MR contrasts during application. Another interesting observation is that all three methods have superior performance over unsupervised I2I methods, demonstrating the benefit of using intra-site paired data in harmonization.

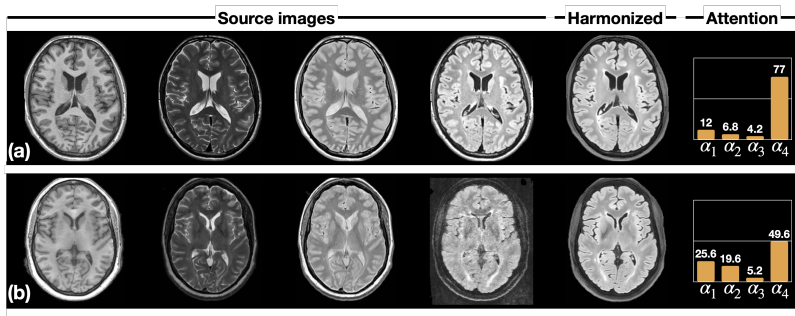


**Fig. 4.** (a) and (b) are two harmonization scenarios where synthetic FLAIR images are generated using  $T_1$ -w,  $T_2$ -w, PD-w, and FLAIR images of each source site, shown from left to right respectively. The learned attentions  $\alpha$  are shown on the right. In (a), all images have high quality, while  $T_1$ -w and FLAIR images in (b) exhibit artifacts.

*Compared with supervised harmonization:* Considering that HACA3 can be trained on a large variety of data, we finally ask ourselves if this could enable HACA3 to outperform supervised harmonization. We compared HACA3 with Dewey et al. [7], a supervised harmonization method that was trained on inter-site paired images from  $S_{11}$  and  $S_{12}$ . We obtained the same evaluation dataset as [7] after communications with the authors. Paired Wilcoxon signed rank test shows that HACA3 outperforms Dewey et al. in SSIM (see Fig. 3) with  $p < 0.01$ .

*Exploring attention on contrast and artifacts:* In Fig. 4, we visualize the learned attention  $\alpha$  in two different harmonization scenarios. In Fig. 4(a), all four source images ( $T_1$ -w,  $T_2$ -w, PD-w, and FLAIR) from Site  $S_{13}$  have good image quality and the target image is a FLAIR image from  $S_{12}$ . In this case, most attention (77%) is on the FLAIR image of the source site. This makes sense, since  $\alpha$  is used to select the corresponding  $\beta$  during harmonization. Figure 4(b) shows another harmonization scenario where the FLAIR image from Site  $S_{19}$  has high artifact levels (noise and motion). In this case, the attention of the FLAIR image has decreased and the other three MR contrasts have increased; the attention model seeks anatomical information from other contrasts to compensate for the poor quality of the FLAIR. As a result, the harmonized FLAIR image shows satisfactory quality with anatomical details preserved during harmonization.

### 3.2 Evaluating HACA3 in downstream tasks

To validate HACA3’s ability to alleviate domain shift, we showcase two different downstream image analysis tasks: WM lesion segmentation and whole brain parcellation. The first task is based on multi-site cross-sectional data and the second task focuses on longitudinal analysis with scanner change and upgrades. **WM lesion segmentation on multi-site data.** As shown in Fig. 5(a), two MS datasets acquired from sites  $S_{11}$  and  $S_{12}$  were used in this experiment. The training data ( $S_{12}$ ) for MS lesion segmentation include  $T_1$ -w (not shown), FLAIR,

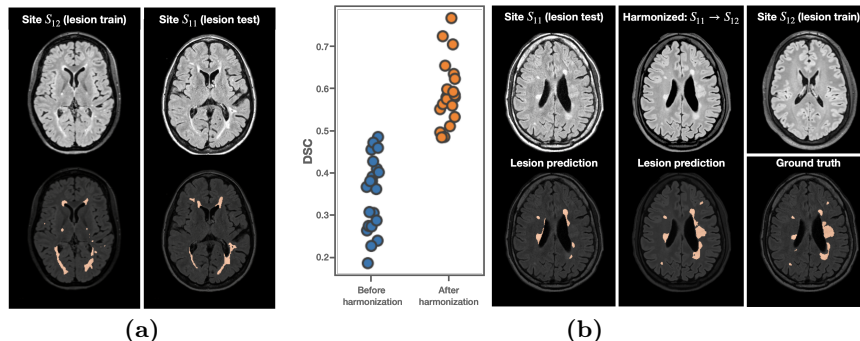


**Fig. 5.** (a) Training and testing sites for WM lesion segmentation with a 3D U-Net. (b) DSC showed improvements after harmonizing images from the novel testing site (Site  $S_{11}$ ) to the lesion training site (Site  $S_{12}$ ). Example images are shown on the right.

**Table 2.** Longitudinal ICCs and  $\sigma_\epsilon^2$  of cGM, WM, and LatV before and after harmonization. Details about each dataset are shown in Table 1 (Sites  $S_3$  to  $S_{10}$ ).

Dataset	# subjects # sessions	Structure	ICC (%)		$\sigma_\epsilon^2$	
			Before	After	Before	After
OASIS3	721 1117	cGM	81.95	<b>95.13</b>	83.6	<b>44.8</b>
		WM	83.54	<b>95.85</b>	64.1	<b>31.9</b>
		LatV	96.37	<b>96.38</b>	25.4	<b>25.2</b>
BLSA	1037 2655	cGM	86.98	<b>96.49</b>	106.9	<b>52.1</b>
		WM	87.35	<b>96.38</b>	133.1	<b>59.3</b>
		LatV	95.96	<b>95.99</b>	46.2	<b>29.7</b>

and expert delineations of WM lesions of 10 subjects. The testing data ( $S_{11}$ ) to evaluate lesion segmentation come from ILLSC 2015 [4], which is publicly available. A 3D U-Net with four downsamplings was trained with MR images and delineations from  $S_{12}$  using a Dice similarity coefficient (DSC) loss.

The 3D U-Net achieved a DSC of  $0.593 \pm 0.072$  (similar to the best results reported in [24] and close to the inter-rater variability of [4]) in a five-fold cross validation on  $S_{12}$ , which it was trained on. However, when the 3D U-Net was applied to  $S_{11}$ , the DSC dropped to  $0.348 \pm 0.089$  due to domain shift. HACA3 was then applied to harmonize images from Site  $S_{11}$  to  $S_{12}$  aiming at alleviating domain shift, and the lesion segmentation was reevaluated. As shown in Fig. 5(b), DSC has improved to  $0.590 \pm 0.075$ , which is similar to the performance on the training site. It is worth noting that WM lesions are particularly difficult to synthesize and characterize due to the large variation in lesion size and location. It is encouraging that HACA3 generates high fidelity images that show effectiveness in WM lesion segmentation both qualitatively and quantitatively.

**Whole brain parcellation on longitudinal data.** We used two public longitudinal datasets, i.e., OASIS3 (Sites  $S_3$  to  $S_6$ ) [13] and BLSA (Sites  $S_7$  to  $S_{10}$ ) [21], to evaluate HACA3 for longitudinal analysis. Number of subjects and sessions of each dataset is shown in Table 2. The same preprocessing was applied



here, followed by a whole brain parcellation on T<sub>1</sub>-w images using [12]. For the cortical GM (cGM), cerebral WM (WM), and lateral ventricles (LatV), a structure-specific linear mixed effects (LME) model  $y_{ij} = a_0 + a_1x_{ij} + b_j + \epsilon_{ij}$  was fitted, where  $x_{ij}$  and  $y_{ij}$  are age and percentage structural volume (structural volume divided by total brain volume) of session  $i$  and subject  $j$ , respectively. We reuse the notations  $x$ ,  $y$ ,  $i$ , and  $j$  to be consistent with the LME literature [10].  $b_j \sim \mathcal{N}(0, \sigma_b^2)$  is the subject-specific bias, and  $\sigma_b^2$  models population variance.  $\epsilon_{ij} \sim \mathcal{N}(0, \sigma_\epsilon^2)$  is the error term modeling noise in observations. Based on the LME, longitudinal intra-class correlations (ICCs) were calculated to characterize the effect of harmonization in longitudinal analysis, i.e.,  $\text{ICC} = \sigma_b^2 / (\sigma_b^2 + \sigma_\epsilon^2)$ , where an ICC close to 0% means the noise in observations is the dominant factor over population difference. An ICC close to 100% indicates most variances are due to the natural population difference rather than noisy observations. Assuming the effect of scanner change and upgrades are alleviated with harmonization, we would expect increased ICCs after harmonization. Table 2 shows that the ICCs and  $\sigma_\epsilon^2$  of all structures from both datasets were improved after harmonization.

## 4 Discussion and Conclusion

In this paper, we challenge common assumptions in current disentangling harmonization methods and propose a novel harmonization framework, HACA3, that respects the natural anatomy differences between MR tissue contrasts. HACA3 also includes an attention mechanism so that it can be trained and applied on any set of MR tissue contrasts and also use contrast and artifact information for better harmonization. Due to the page limit, we did not present the learned artifact representation but note that, in addition to its use in harmonization, this information may be useful for MR image quality control. We also note that while attention is currently applied to entire images, in the future it may be applied regionally to address local artifacts or contrast anomalies. Diverse MR datasets show that HACA3 achieves state-of-the-art performance compared with both supervised and unsupervised harmonization. Downstream tasks in WM lesion segmentation and whole brain parcellation demonstrate that HACA3 can be applied in various neuroimage analysis tasks for more consistent measurements.

## Acknowledgements

The authors thank BLSA participants. This work was supported in part by the Intramural Research Program of the NIH, National Institute on Aging, in part by the NINDS grants R01-NS082347 (PI: P. A. Calabresi) and U01-NS111678 (PI: P. A. Calabresi), and in part by the TREAT-MS study funded by the Patient-Centered Outcomes Research Institute (PCORI/MS-1610-37115).

## References

1. IXI Brain Development Dataset. <https://brain-development.org/ixi-dataset/>

2. Adeli, E., et al.: Representation learning with statistical independence to mitigate bias. In: Proceedings of the IEEE/CVF Winter Conference on Applications of Computer Vision. pp. 2513–2523 (2021)
3. Biberacher, V., et al.: Intra-and interscanner variability of magnetic resonance imaging based volumetry in multiple sclerosis. *NeuroImage* **142**, 188–197 (2016)
4. Carass, A., et al.: Longitudinal multiple sclerosis lesion segmentation data resource. *Data in brief* **12**, 346–350 (2017)
5. Chartsias, A., et al.: Disentangled representation learning in cardiac image analysis. *Medical Image Analysis* **58**, 101535 (2019)
6. Clark, K.A., et al.: Impact of acquisition protocols and processing streams on tissue segmentation of T1 weighted MR images. *NeuroImage* **29**(1), 185–202 (2006)
7. Dewey, B.E., et al.: DeepHarmony: a deep learning approach to contrast harmonization across scanner changes. *Magnetic Resonance Imaging* **64**, 160–170 (2019)
8. Dewey, B.E., et al.: A disentangled latent space for cross-site MRI harmonization. In: International Conference on Medical Image Computing and Computer-Assisted Intervention. pp. 720–729 (2020)
9. Dewey, B.E., et al.: Chapter 11 - Medical image harmonization through synthesis. In: Biomedical Image Synthesis and Simulation, pp. 217–232. The MICCAI Society book Series, Academic Press (2022)
10. Erus, G., et al.: Longitudinally and inter-site consistent multi-atlas based parcellation of brain anatomy using harmonized atlases. *NeuroImage* **166**, 71–78 (2018)
11. Huang, X., et al.: Multimodal unsupervised image-to-image translation. In: Proceedings of the European Conference on Computer Vision. pp. 172–189 (2018)
12. Huo, Y., et al.: 3D whole brain segmentation using spatially localized atlas network tiles. *NeuroImage* **194**, 105–119 (2019)
13. LaMontagne, P.J., et al.: OASIS-3: Longitudinal neuroimaging, clinical, and cognitive dataset for normal aging and Alzheimer disease. medRxiv (2019)
14. Liu, M., et al.: Style transfer using generative adversarial networks for multi-site MRI harmonization. In: International Conference on Medical Image Computing and Computer-Assisted Intervention. pp. 313–322. Springer (2021)
15. Liu, Y., et al.: Disentangled representation learning for OCTA vessel segmentation with limited training data. *IEEE Transactions on Medical Imaging* (2022)
16. Locatello, F., et al.: Challenging common assumptions in the unsupervised learning of disentangled representations. In: International Conference on Machine Learning. pp. 4114–4124. PMLR (2019)
17. Ouyang, J., et al.: Representation disentanglement for multi-modal brain MRI analysis. In: International Conference on Information Processing in Medical Imaging. pp. 321–333. Springer (2021)
18. Park, T., et al.: Contrastive learning for unpaired image-to-image translation. In: European Conference on Computer Vision. pp. 319–345. Springer (2020)
19. Prince, J.L., Links, J.M.: Medical imaging signals and systems. Pearson Prentice Hall Upper Saddle River (2006)
20. Reinhold, J.C., et al.: Evaluating the impact of intensity normalization on MR image synthesis. In: Medical Imaging 2019: Image Processing. vol. 10949, p. 109493H. International Society for Optics and Photonics (2019)
21. Resnick, S.M., et al.: One-year age changes in mri brain volumes in older adults. *Cerebral Cortex* **10**(5), 464–472 (2000)
22. Ronneberger, O., et al.: U-Net: convolutional networks for biomedical image segmentation. In: International Conference on Medical Image Computing and Computer-Assisted Intervention. vol. 9351, pp. 234–241 (2015)



23. Tian, D., et al.: A deep learning-based multisite neuroimage harmonization framework established with a traveling-subject dataset. *NeuroImage* p. 119297 (2022)
24. Tohidi, P., et al.: Multiple sclerosis brain lesion segmentation with different architecture ensembles. In: *Medical Imaging 2022: Biomedical Applications in Molecular, Structural, and Functional Imaging*. vol. 12036, pp. 578–585. SPIE (2022)
25. Tustison, N.J., et al.: N4ITK: improved N3 bias correction. *IEEE Transactions on Medical Imaging* **29**(6), 1310–1320 (2010)
26. Vaswani, A., et al.: Attention is all you need. *Advances in Neural Information Processing Systems* **30** (2017)
27. Wang, Z., et al.: Image quality assessment: from error visibility to structural similarity. *IEEE Transactions on Image Processing* **13**(4), 600–612 (2004)
28. Zhao, C., et al.: SMORE: a self-supervised anti-aliasing and super-resolution algorithm for MRI using deep learning. *IEEE Transactions on Medical Imaging* **40**(3), 805–817 (2020)
29. Zhu, J.Y., et al.: Unpaired image-to-image translation using cycle-consistent adversarial networks. In: *Proceedings of the IEEE International Conference on Computer Vision*. pp. 2223–2232 (2017)
30. Zuo, L., et al.: Synthesizing realistic brain MR images with noise control. In: *International Workshop on Simulation and Synthesis in Medical Imaging*. pp. 21–31 (2020)
31. Zuo, L., et al.: Information-based disentangled representation learning for unsupervised MR harmonization. In: *International Conference on Information Processing in Medical Imaging*. pp. 346–359. Springer (2021)
32. Zuo, L., et al.: Unsupervised MR harmonization by learning disentangled representations using information bottleneck theory. *NeuroImage* **243**, 118569 (2021)
33. Zuo, L., et al.: Disentangling a single MR modality. In: *Data Augmentation, Labelling, and Imperfections*. pp. 54–63. Springer Nature Switzerland (2022)